Stator Inter-Turn Fault Detection in Permanent Magnet Machines Using PWM Ripple Current Measurement

Bhaskar Sen, *Student Member, IEEE*, and Jiabin Wang, *Senior Member, IEEE*

***Abstract*— The paper proposes a novel method of inter-turn fault detection based on measurement of pulse width modulation (PWM) ripple current. The method uses the ripple current generated by the switching inverter as a means to detect inter-turn fault. High frequency impedance behavior of healthy and faulted windings are analyzed and modeled, and ripple current signature due to inter-turn faults is quantified. A simple analogue circuit is designed to extract the PWM ripple current via a band-pass filter and a root-mean-square (RMS) detector for fault detection. In addition, this method can also identify the faulted phase, which can be used for fault mitigation strategies. The method is tested experimentally on a five phase permanent magnet machine drive.**

***Index Terms*— Condition monitoring, fault diagnosis, fault location, switching frequency fault detection, pulse width modulation inverters, permanent magnet machines.**

NOMENCLATURE

V_{dc}	DC link voltage
V_{iN}	Inverter i^{th} pole voltage with respect to minus rail
M_i	modulation index of the i^{th} phase
ω_c	angular frequency of PWM carrier waveform
ω_f	angular frequency of fundamental waveform
J_0	Bessel function of 0^{th} order
J_n	Bessel function of n^{th} order
L	Self inductance
R	Stator resistance
R_{fault}	External fault resistance
L_m	Mutual inductance between healthy and faulted winding
E_i	Electro-motive voltage (EMF) of the i^{th} phase
p	Number of pole pairs
N	Total number of turns / phase
N_f	Total number of faulted turns
Z_i	Impedance of the i^{th} phase
$Y_{h,expt}$	Experimentally extracted admittance of healthy winding
$Y_{f,expt}$	Experimentally extracted admittance of faulted winding
j	complex number (sqrt(-1))

SUBSCRIPTS

h or f	healthy or faulty part of winding

Manuscript received March 06, 2015; revised July 24, 2015; accepted October 8, 2015.

This work was supported in part by the European ENIAC Joint Undertaking under the MotorBrain project.

The authors are with the Electrical Machines and Drives Research Group, Department of Electronic and Electrical Engineering, The University of Sheffield, Sheffield, S1 3JD, UK (email: elp11bs@sheffield.ac.uk).

I. INTRODUCTION

PERMANENT magnet (PM) machines are increasing being favored as the machine of choice for electric vehicle application due to their high power density, and high efficiency [1], [2]. However, due to presence of magnets in the rotor, electrical faults must be quickly detected and mitigating controls initiated to prevent catastrophic failure of the machine. Such a functionality commonly known as "limp-home" mode [3] is essential for providing high degree of availability, and reliability demanded in safety critical application such as electric vehicles. For providing high availability in electric vehicles, reliable diagnostics of motor operational states and health is essential. Internal combustion engines based vehicles already have diagnostics features which provides users with an early warning of a problem within the engine [4]. A similar functionality would be highly desirable in electric vehicles.

Several surveys on reliability of industrial motors conducted by Electric Power Research Institute EPRI [5] and IEEE [6]–[9] concluded that stator winding failures accounts for about 21-37% of faults in electrical machines. One of the leading causes of winding failure are inter-turn short-circuit failures which are especially critical, since it leads to a large circulating current in the faulted turns [10]. This gives rise to a local hot spot which can cause further insulation failures and ultimately leading to a complete failure of the winding as a phase-ground or phase-to-phase fault [11]. The large circulating current in the faulted turns can also produce irreversible demagnetization of the magnets [12].

Stator inter-turn fault detection has been subject to intense investigation and numerous literatures exist on the topic. Detection schemes [13], [14] are broadly divided into fundamental quantity based [15]–[21] detection, high frequency based [22]–[24] detection and motor current signature analysis (MCSA) [25]–[27]. Most of the methods

under MCSA are computationally intensive since they rely on performing fast Fourier transformation (FFT) to determine harmonic components and fault signature. High frequency signal injection methods on the other hand, inject high frequency (HF) signal in the inverter voltage command and perform synchronous demodulation of currents in software to determine stator turn fault. In [22] a high frequency signal is added in the *dq* control voltages and the high frequency currents so obtained is demodulated in *dq* frame and the negative sequence component extracted to form the fault index. In [24] the method of [22] is improved further by using lookup table based calibration of the *dq* high frequency signal to reduce effect of magnetic saliency induced by load variation from affecting the detection. However, signal injection method introduces additional noise in the current and increases acoustic emissions of the motor-drive system [28], [29]. In addition, most of the methods fail to identify the faulted phase which is of importance in a multi-phase machine in order to initiate fault mitigation and fault tolerant operation.

Most PM machines are fed through a pulse-width modulated (PWM) drive. The drive is a natural source of high frequency signal injection into the motor due to its switching. It is this inherent source of HF signal injection that is explored in this paper for detection of turn fault. The proposed method uses the PWM ripple current generated by the drive to determine the presence of turn fault without the need to modify or inject additional HF signal [30]. The method is also able to identify the faulted phase which is essential to implement fault mitigation strategies.

II. Machine Modeling Under Turn Fault

The machine under consideration is a 10-slot, 12-pole, 5 phase surface mounted permanent magnet (SPM) machine. Fig. 1 shows the geometry of the machine. This topology, also known as alternate tooth wound SPM machine, is inherently fault tolerant due to both physical and magnetic separation of the coils of the winding i.e., virtually no mutual magnetic coupling between phases. Fig. 2 shows the schematic of a single winding of the machine under the turn fault condition with N_f faulted turns out of a total N number of turns.

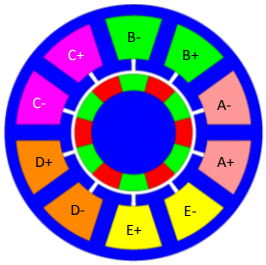

Fig. 1: Geometry of 10-slot, 12-pole SPM machine

In order to evaluate the ripple current characteristics under PWM operation, it is necessary to determine the high frequency admittance of the winding under healthy and fault conditions. For the machine under study, the high frequency admittance can be obtained using (1) by setting the electromotive force (EMF) voltage components to zero in Fig. 2, where R_h, R_f, L_h and L_f are the resistance and inductance of the healthy and fault turns, respectively and L_m is the mutual inductance between the two winding parts. R_{fault} is assumed zero in this analysis for sake of simplicity.

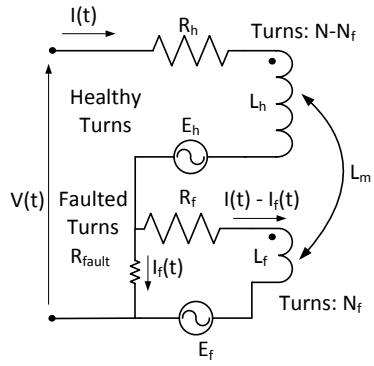

Fig. 2: Schematic of winding under turn fault

$$Y(j\omega)=\frac{I(j\omega)}{V(j\omega)}=\frac{1}{\left(R_h+j\omega L_h+\dfrac{\omega^2 L_m{}^2}{R_f+j\omega L_f}\right)} \quad (1)$$

The parameters of the machine under healthy and fault conditions are given in Table I and Table II obtained by employing an analytical solution of the air-gap magnetic field and a slot-leakage model as described in detail in [10]. Since the machine under study employs a SPM topology in which saturation level is quite low, these parameters are constant. For machines with high level of saturation, the derivation is still valid given that the ripple current is small, and the parameters can be piece-wise linearized.

TABLE I
MACHINE DATA

Specification	Value	Specification	Value
No. of phases	5	Phase Resistance	0.68Ω
No. of poles	12	Phase Inductance	2.8mH
No. of slots	10	Rated Current	6.0 A
Turns per phase	62	Maximum Speed	3000 r/min
Back-EMF(peak)	37V	Rated Torque	1.86 Nm
DC Voltage	60V	Switching Frequency	10kHz

TABLE II
MACHINE DATA UNDER FAULT

Parameter	Fault Condition	
N_f	2 turn fault	20 turn fault
R_h	0.66Ω	0.46Ω
R_f	0.02Ω	0.22Ω
L_h	2.6mH	1.3mH
L_f	2.8μH	0.28mH
L_m	83μH	0.6mH

Fig. 3 shows the comparison of the theoretical and experimentally measured admittance of the winding under locked rotor condition using an impedance analyzer (Hioki IM3533-01). It can be observed that under the fault conditions the admittance increases particularly in the frequency range of 10-20 kHz compared to healthy condition. It is also to be noted that the admittance predicted by theory is different from

that obtained from experiments and is especially evident in case of 2-turn fault. The difference between the theoretical and measured admittance is expected and attributed to extra impedance introduced by the external leads to create the fault, and iron losses (eddy, hysteresis loss) as well as high frequency losses due to skin and proximity effects in the measured data which is not accounted for in the simple theoretical model. Also, as the number of faulted turn increases from 0 (healthy) to 2 turns and finally to 20 turn the admittance progressively increases above 10 kHz. Higher admittance translates to lower impedance and hence higher currents for the same voltage. It is to be observed that although there is difference between experimental and simplified theoretical predictions both the measurement and prediction point towards an increase of high frequency admittance and this is due to the shorted turns which reduce the overall impedance of the winding.

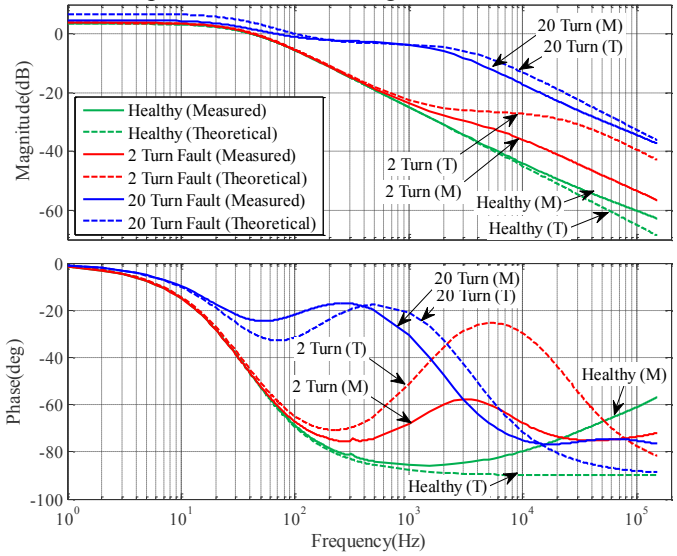

Fig. 3: Admittance (Y) magnitude and phase of winding under healthy, 2 turn and 20 turn fault. Theoretical (T) – dashed, Measured (M) – solid

Therefore, if the motor can be excited with a voltage in the frequency range of 10 kHz-20 kHz, the measured current will show an increase under fault condition which can be used as a measure to detect turn fault. A PM motor is usually fed from a PWM drive which generates not only the fundamental voltage for the motor, but also switching voltage ripple at the terminals. The resultant PWM current ripple can be used as detector for inter-turn faults. For the purpose of simulation in this paper a sine-PWM drive, with a switching frequency of 10 kHz is assumed.

In order to represent the winding behavior more realistic to the actual physical measurements, a hybrid modeling approach is employed. This entails using the impedance/admittance data obtained from experimental measurement and combining it with the analytical model to obtain a more accurate representation of the actual circuit condition. In order to use the experimental data in simulation the experimental measurement is fitted with an approximate transfer function (2) using least squares fitting to obtain $Y_{f,expt}(s)$ and $Y_{h,expt}(s)$ for faulted and healthy winding respectively.

$$Y(s)=\frac{b_5s^5+b_4s^4+b_3s^3+b_2s^2+b_1s^1+b_0}{a_5s^5+a_4s^4+a_3s^3+a_2s^2+a_1s^1+a_0} \quad (2)$$

Fig. 4 and Fig. 5 show the transfer function fitting for healthy condition and for 2-turn and 20-turn short circuit conditions, respectively.

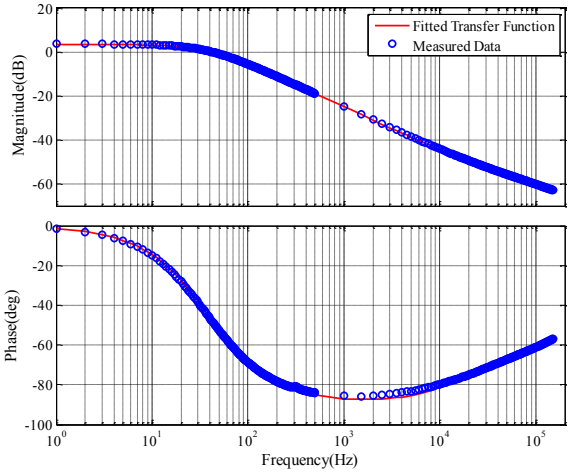

Fig. 4: Fitted Admittance Function ($Y_{h,expt}(s)$) for Healthy Condition

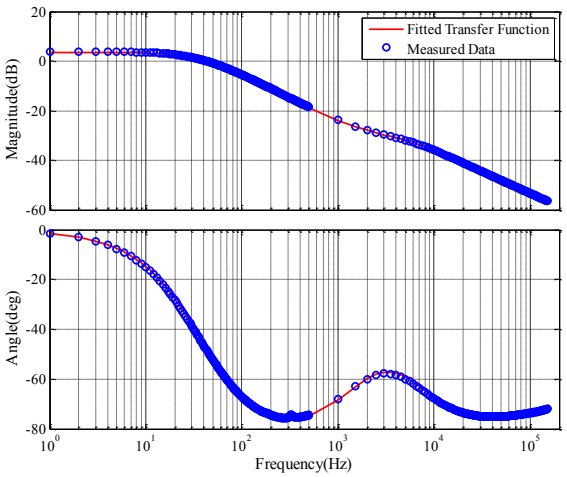

Fig. 5: Fitted Admittance function ($Y_{f,expt}(s)$) for (a) 2 turn and (b) 20 turn fault condition

The circuit equations of a generic faulted winding as shown in Fig. 2 can be expressed in s domain and are given by (3)-

(4). I(s)-I_f(s) can be eliminated from the voltage equation (3) to obtain (5)-(6).

$$R_{fault}I_f(s)=\left(R_f+sL_f\right)\left(I(s)-I_f(s)\right)+sL_mI(s)+E_f(s) \tag{3}$$

$$V(s)=\left(R_h+sL_h\right)I(s)+sL_m\left(I(s)-I_f(s)\right)+E_h(s) +R_{fault}I_f(s) \tag{4}$$

$$V(s)=\frac{R_{fault}-sL_m}{sL_f+R_f+R_{fault}}E_f(s)+E_h(s) +I(s)\left(R_h+s\left(L_h+L_m\right)+\frac{\left(R_{fault}-sL_m\right)\left(s\left(L_f+L_m\right)+R_f\right)}{sL_f+R_f+R_{fault}}\right) \tag{5}$$

$$V(s)=\frac{1}{Y_f(s)}I(s)+\frac{R_{fault}-sL_m}{sL_f+R_f+R_{fault}}E_f(s)+E_h(s) \tag{6}$$

Since the measured winding admittance is a high order transfer function, the model equation needs to be modified to account for the high frequency losses. A close look at (6) reveals that the first term corresponds both to the high frequency and low frequency admittance ($Y_f(s)$), whereas the other two terms are only related to the back-EMF components. Hence, it is possible to substitute the experimentally derived admittance instead of the theoretically derived one, resulting in the hybrid model equation for the faulted phase in (7). Therefore, (7) contains a part of parameters obtained through experiment and the rest is calculated from theoretical model, and is therefore referred to as a hybrid model.

$$V(s)=\frac{1}{Y_{f,\text{expt}}(s)}I(s)+\frac{R_{fault}-sL_m}{sL_f+R_f+R_{fault}}E_f(s)+E_h(s) \tag{7}$$

In the 5-phase experimental motor considered in this paper, the winding fault is assumed to occur in phase 4 as shown in Fig. 6. Thus, (7) can be re-written as (8) noting that $E_h = E_i - E_f$ where E_i is the healthy back-EMF of the ith phase. Zero sequence voltage (V_{nN}) is added into (8)-(9) to account for the fact that the voltages generated by the inverter are referred with respect to the negative DC supply N while the phase voltages are referred to the floating neutral 'n' of the motor. The model for other healthy windings can be written as (9). In order to simulate the system the zero sequence voltage V_{nN} needs to be eliminated from the model equations. By summing (8)-(9) over all phases, and noting that the sum of the phase currents is zero for a star connected system, V_{nN} can be obtained as given by (10). Substituting (10) in (8)-(9), the final model equations (11)-(12) can be obtained.

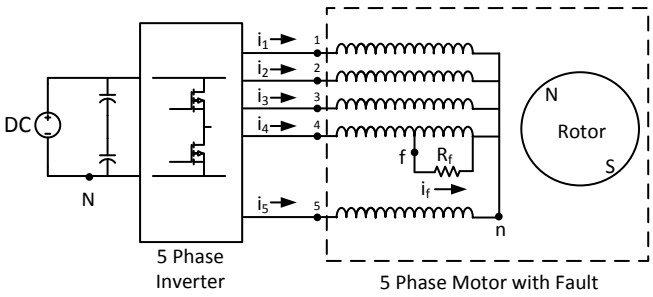

Fig. 6: Schematic representation of 5 phase SPM machine with turn fault on a single phase

$$V_{iN}(s)=\frac{1}{Y_{f,\text{expt}}(s)}I_i(s)+\frac{R_{fault}-sL_m}{sL_f+R_f+R_{fault}}E_f(s) +E_i(s)-E_f(s)+V_{nN}\quad;\ i=4 \tag{8}$$

$$V_{iN}(s)=\frac{1}{Y_{h,\text{expt}}(s)}I_i(s)+E_i(s)+V_{nN}\ ;\ \forall i\neq 4 \tag{9}$$

$$5V_{nN}=-\left(\frac{1}{Y_{f,\text{expt}}(s)}-\frac{1}{Y_{h,\text{expt}}(s)}\right)I_4(s) -\frac{R_{fault}-sL_m}{sL_f+R_f+R_{fault}}E_f(s)+E_f(s)+\sum_{i=1}^{5}V_{iN}(s) \tag{10}$$

$$V_{iN}(s)=\left(\frac{4}{5}\frac{1}{Y_{f,\text{expt}}(s)}+\frac{1}{5}\frac{1}{Y_{h,\text{expt}}(s)}\right)I_i(s)+E_i(s) -\frac{4}{5}E_f(s)-\frac{4}{5}\frac{sL_m-R_{fault}}{sL_f+R_f+R_{fault}}E_f(s)+\frac{1}{5}\sum_{i=1}^{5}V_{iN}(s);\ i=4 \tag{11}$$

$$V_{iN}(s)=\frac{1}{Y_{h,\text{expt}}(s)}I_i(s)+\frac{1}{5}\left(\frac{sL_m-R_{fault}}{sL_f+R_f+R_{fault}}+1\right)E_f(s) -\frac{1}{5}\left(\frac{1}{Y_{f,\text{expt}}(s)}-\frac{1}{Y_{h,\text{expt}}(s)}\right)I_4(s)+E_i(s)+\frac{1}{5}\sum_{i=1}^{5}V_{iN}(s);\forall i\neq 4 \tag{12}$$

III. PWM Current Ripple Based Detector Design

In order to extract the high frequency current, first an appropriate frequency band needs to be selected. In order to aid the design process, the harmonic currents can be analytically calculated under different operating conditions in steady state assuming ideal sine PWM. The PWM harmonic voltages for sine triangle modulation can be calculated using (13) [31]. V_{dc} is assumed as 140V for the calculation, which is the maximum rated DC link voltage of the test inverter. Harmonic line currents can then be calculated using (14).

$$V_{i,h}(t)=\frac{2V_{dc}}{\pi}\sum_{m=1}^{\infty}\frac{1}{m}J_0\left(m\frac{\pi}{2}M_i\right)\cos\left(m\omega_c t\right)\sin\left(m\frac{\pi}{2}\right) +2\frac{V_{dc}}{\pi}\sum_{m=1}^{\infty}\sum_{\substack{n=-\infty\\ n\neq 0}}^{\infty}\left[\begin{array}{l}\frac{1}{m}J_n\left(m\frac{\pi}{2}M_i\right)\cos\left(m\omega_c t+n\left(\omega_f t+\theta_i\right)\right)\\ .\sin\left(\left(m+n\right)\frac{\pi}{2}\right)\end{array}\right] \tag{13}$$

$$\begin{bmatrix} V_{1,h}-V_{2,h} \\ V_{2,h}-V_{3,h} \\ V_{3,h}-V_{4,h} \\ V_{4,h}-V_{5,h} \end{bmatrix} = \begin{bmatrix} Z_1 & -Z_2 & 0 & 0 \\ 0 & Z_2 & -Z_3 & 0 \\ 0 & 0 & Z_3 & -Z_4 \\ Z_5 & Z_5 & Z_5 & Z_4+Z_5 \end{bmatrix} \begin{bmatrix} I_{1,h} \\ I_{2,h} \\ I_{3,h} \\ I_{4,h} \end{bmatrix} \quad (14)$$

Fig. 7(a) shows the predicted RMS harmonic current plots for each phase using measured motor impedance, when phase 4 has a 2-turn fault at the maximum current of 6A when only 10 kHz carrier frequency sidebands are considered and Fig. 7(b) shows the RMS harmonic current plots when both 10 kHz and 20 kHz carrier frequency sidebands are considered. It is evident from the plots that by considering both the 10 kHz and 20 kHz current ripple a greater magnitude and separation between the faulted phase and healthy phases can be obtained specially in low speed range. This will also improve signal to noise ratio. Thus, a pass-band of 10-20 kHz is selected for optimal detection of fault. It is to be noted in Fig. 7 that the ripple current in the other healthy phases are not same under fault condition. This is expected since the fault causes fundamental voltage unbalance which changes the line-line voltage in a star connected system which in turn affects the PWM ripple current of each phase.

The separation in RMS current ripple between faulted and healthy phases allow for easy identification of fault. It should be noted that the harmonic voltages and hence the harmonic currents are a function of modulation index and therefore as speed or load change the harmonic currents also vary.

Extraction of harmonic currents can be done in many different ways. One direct approach is the use of high speed sampling of the stator current waveform and application of signal processing to extract the harmonics. However, the ripple current is very small compared to the fundamental current and therefore the ADC employed would have to have a high resolution (>16 bits) to be able to measure the PWM ripple current accurately. Moreover, the sampling frequency of the ADC has to be at least 5-10 times the highest ripple current frequency and the corner frequency of the anti-alias filter has to be increased accordingly. Therefore, although this approach has the benefit of flexibility of application of advanced signal processing to extract harmonic currents it requires high speed, high resolution ADC's and advanced DSP processor to perform the signal acquisition and processing.

Due to processing limitations of the control hardware, an alternate approach is employed in this paper wherein the RMS value of the PWM ripple current is obtained by using an analog circuit. RMS ripple current so extracted is of low frequency and can be easily sampled by the DSP using the same ADC sample rate (10 kHz) as that employed for current controller. The analog signal processing chain is shown in Fig. 8, consisting of a second order band-pass filter, RMS detector and output buffer. The band-pass (BP) filter must provide sufficient attenuation at fundamental frequency to prevent changes in fundamental current from affecting the result of the RMS detector. For the particular motor, a stop-band attenuation of -38dB (at 300Hz) is found to be adequate to remove the fundamental current influence. The pass-band gain of 20 dB is found to be sufficient for the detection. The bode gain plot of the BP filter is given in Fig. 9. The output buffer provides a further gain of +26dB.

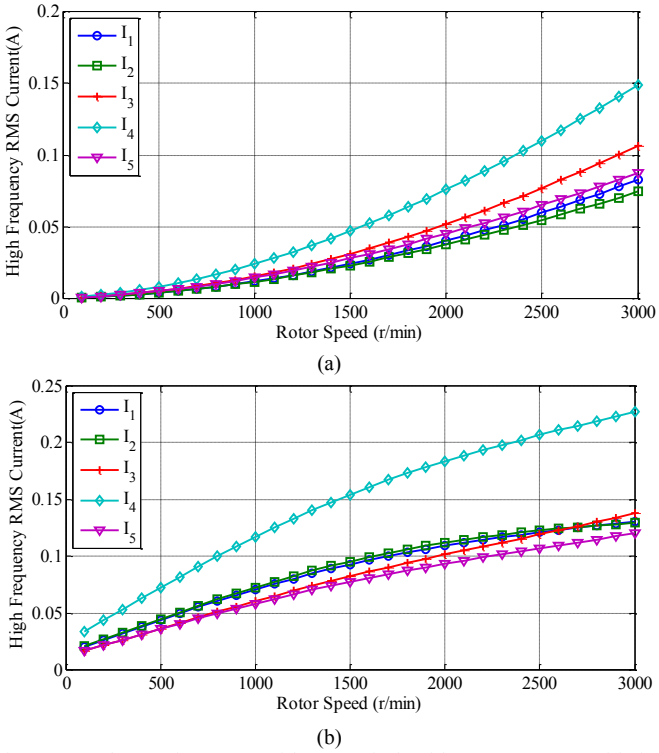

Fig. 7: RMS harmonic current with 2 turn fault with V_{dc} = 140V considering (a) only 10kHz carrier and sidebands, (b) 10kHz and 20kHz carrier frequency harmonics and sidebands.

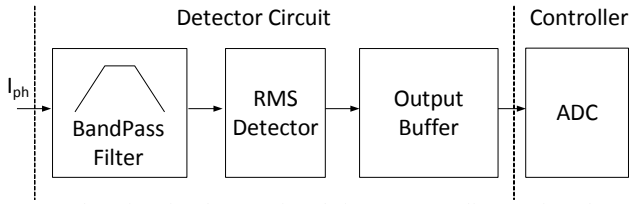

Fig. 8: HF detection signal processing chain. ADC sampling rate is 10 kHz.

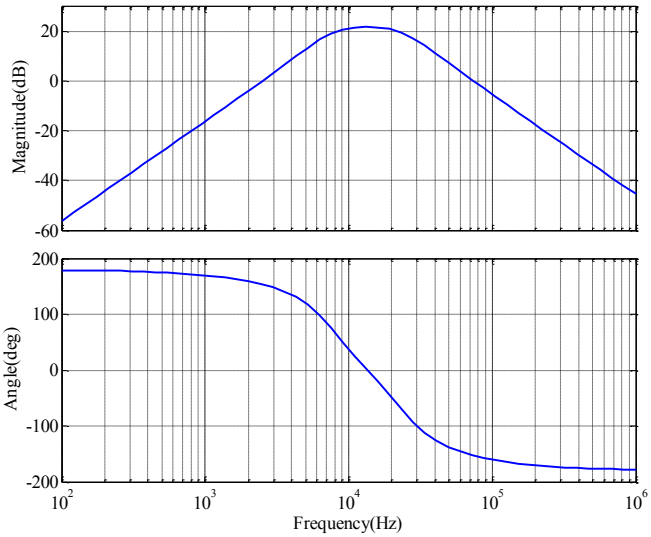

Fig. 9: Band-pass Filter Bode Plot

IV. Simulation Results

Fig. 10 shows the simulation results obtained from the model derived in foregoing section connected to a current controlled voltage source inverter at rotor speed of 500 r/min with i_q = 6A under a 2 turn fault condition with V_{dc} = 60V. Standard *dq* based current control as employed in [32] is utilized to control the fundamental current. The current sensor gain is set at 1/40 corresponding to the sensor used in hardware. The difference in high frequency ripple can be observed in the actual phase current plots, and is clearly identifiable in the detector output shown in Fig. 11, where phase -4 shows a higher output than the rest of the phases and hence is identified as the phase with fault. The ripple in the detector output is caused by the currents in sidebands of the carrier frequency which give rise to a beat frequency at twice the fundamental frequency.

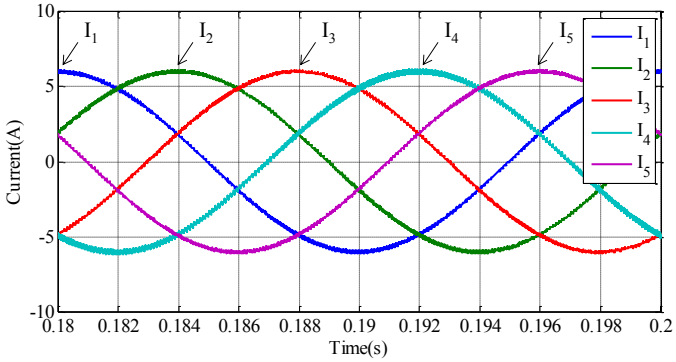

Fig. 10: Simulated phase currents with a 2 turn fault in phase-4 at rotor speed of 500 r/min.

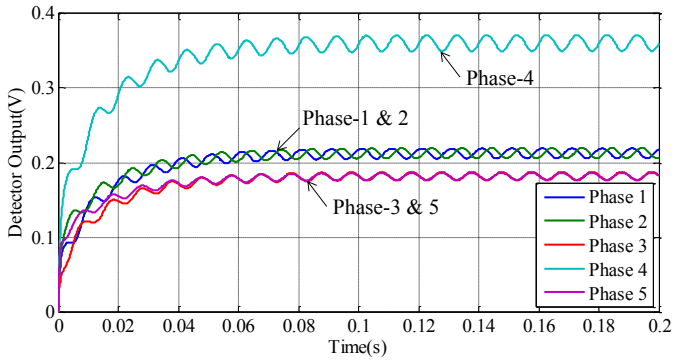

Fig. 11: Simulated detector output with a 2 turn fault in phase-4 at rotor speed of 500 r/min.

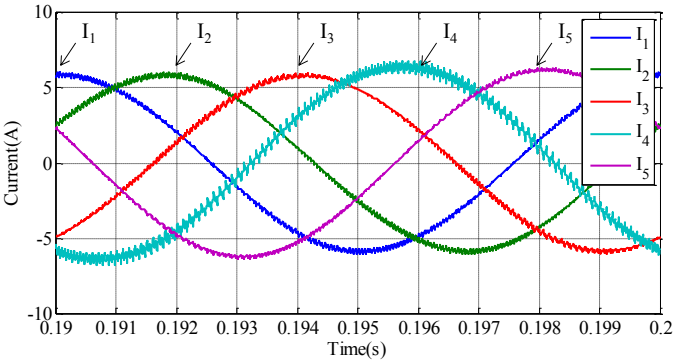

Fig. 12: Simulated phase currents with a 20 turn fault in phase-4 at rotor speed of 1000 r/min.

Fig. 12 shows simulation results obtained at rotor speed of 1000 r/min with i_q = 6A under 20 turn fault condition with V_{dc} = 60V. The phase currents are slightly unbalanced and this is expected since 20 turn fault introduces unbalance which cannot be completely compensated using conventional positive sequence *dq* controller. The difference in the ripple current is quite apparent and is expected at higher speeds and higher fault ratios. Fig. 13 shows the detector output and phase 4 can be clearly identified.

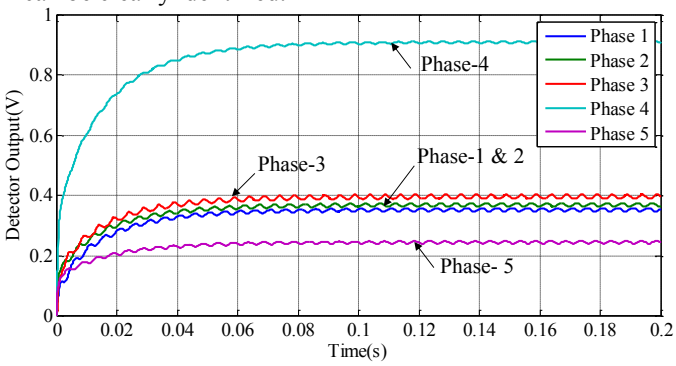

Fig. 13: Simulated detector output with a 20 turn fault in phase-4 at rotor speed of 1000 r/min.

V. Circuit Implementation

Fig. 14 shows the schematic of the analog signal processing circuit. The current signal from the transducer is first fed to the high pass filter (HPF) U1 and then through the low pass filter (LPF) U2 into the RMS detector U3 and finally into the ADC buffer U4. The LEM current sensor selected for the inverter is LTS-25P which gives a unipolar output and therefore the entire HF signal chain is designed to operate on unipolar supply. To realize the LPF and HPF transfer functions multiple-feedback topology is used. OPA364 is selected as the operational amplifier (opamp) for the circuit due to its excellent BW and low offset voltage and is suitable for unipolar circuit realization. The RMS detector is LTC1968 which is a precision wide bandwidth, RMS-to-DC converter from Linear Technology [33]. LTC1968 has a differential input range of 1Vpk and to avoid saturating the RMS detector under worse case fault, a gain of 20dB is selected for the band-pass divided equally over the HPF and LPF. Finally the ADC buffer provides additional gain of +26dB on the detected RMS value. A point to be noted for the signal chain is that the sequence of the block in the chain is critical to obtaining the desired performance. For example, swapping the position of HPF and LPF in the signal chain would saturate the opamps in the circuit although the transfer function of the circuit would have remained unaltered. This is because the LPF will pass the fundamental current signal with a gain of +10dB and will saturate the opamps in the circuit.

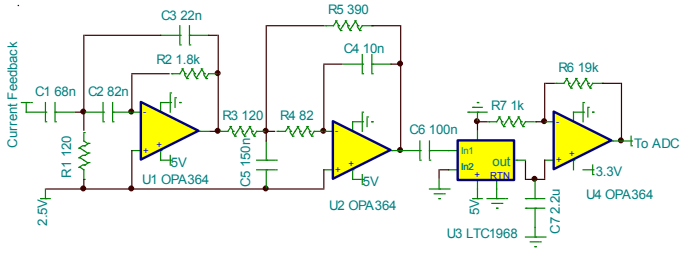

Fig. 14: Detector Circuit Implementation

VI. Experimental Testing

To test the fault detection technique a test-rig was fabricated, to create turn faults and study the performance of the detection algorithms. Fig. 15 shows the test-rig. The test-rig comprises of a dynamometer connected to the 5-phase machine which has two separate taps on one of its phase windings (Phase 4 – faulted phase). 2 turn and 20 turn fault can be created to test detector performance. An incremental encoder is used for rotor position feedback. A five phase MOSFET inverter is used to control the test motor. The inverter is controlled through a floating point TI DSP board (EzDSP F28335). Commands to the DSP board is issued through either CAN interface using LabView or the USB connection via the TI Code Composer studio. DC link voltage is set at 60V for the experiments. Standard *dq* based current control as employed in [32] is utilized to vary the fundamental frequency current loading of the test machine.

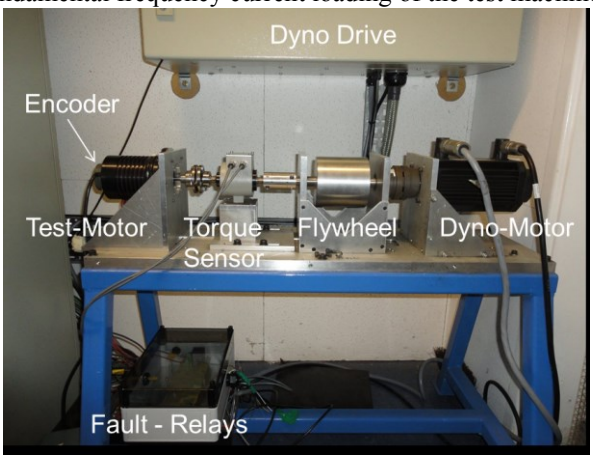

Fig. 15: Dynamometer setup with test motor with faults

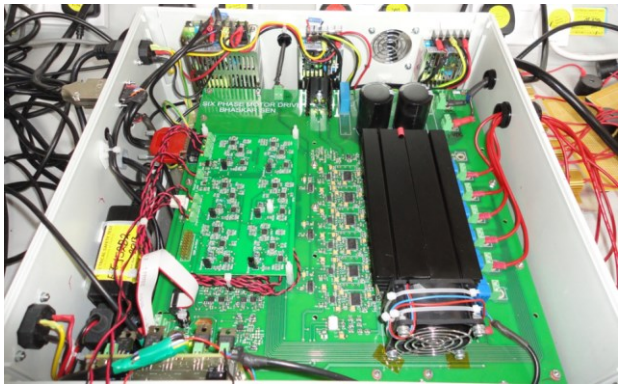

Fig. 16: Inverter with HF detection board

Fig. 17(a) and (b) show the detector output at i_q = 6A at 2 turn fault and rotor speed of 500 r/min and 1000 r/min, respectively, captured using yokogawa oscilloscope, where Ch4 is the detector output of the faulted phase. It can be observed that each detector channel has a different output before fault is initiated. This is to be expected since each phase has slightly different impedances due to fabrication process, and there is variation in each detector channel. This variation can be easily compensated by implementing a software based calibration explained in the next section. During fault, phase -4 detector output shows clear change of output from the pre-fault level.

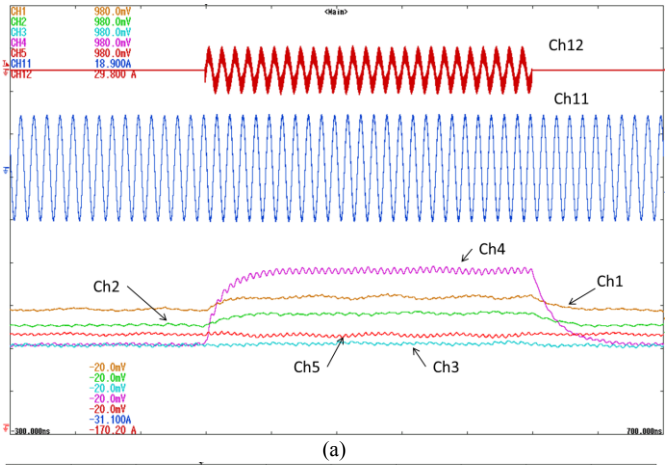

(a)

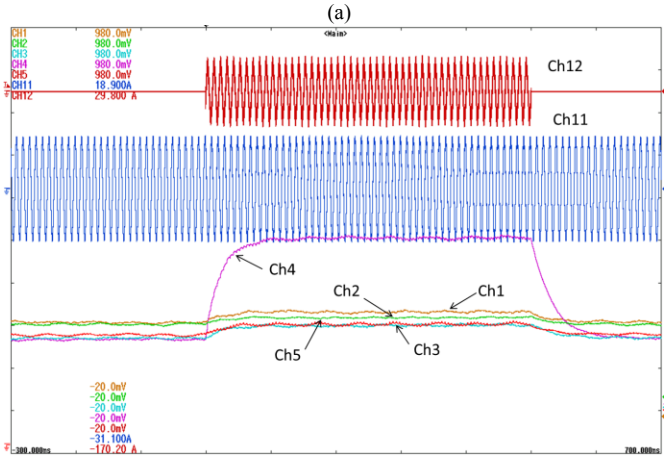

(b)

Fig. 17: Detector output with 2 turn fault in phase-4 with i_q =6A at (a) 500 r/min, (b) 1000 r/min. Ch1- Ch5 - detector outputs for phase 1 through phase 5 respectively (100mV/div), Ch11 - phase 4 current (5A/div), Ch12 is fault current (20A/div). Time scale – 100ms/div

Fig. 18 (a) and (b) show the detector output at i_q = 6A with 20 turn fault and rotor speed of 500 r/min and 1000 r/min, respectively. Similar response to 2 turn fault case with different output levels can be clearly observed.

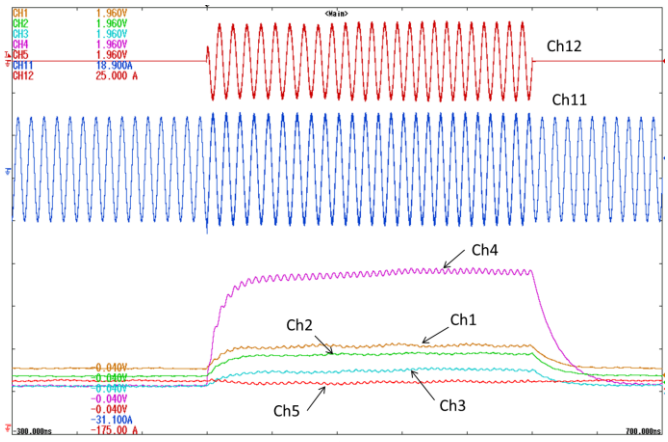

(a)

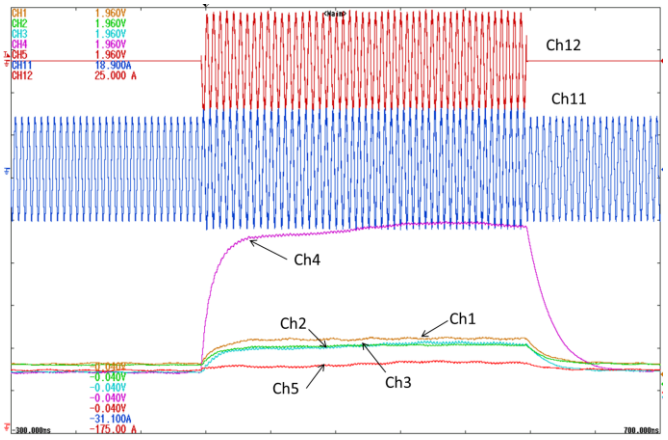

(b)

Fig. 18: Detector output with 20 turn fault in phase-4 with i_q=6A at (a) 500 r/min, (b) 1000 r/min. Ch1-Ch5 - detector outputs for phase 1 through phase 5 respectively (200mV/div), Ch11 - phase 4 current (5A/div), Ch12 is fault current (20A/div). Time scale – 100ms/div

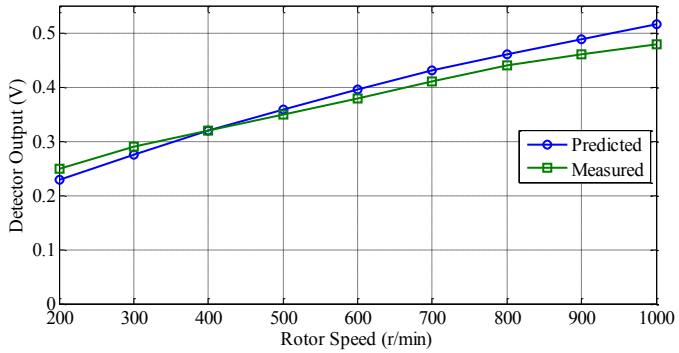

(a)

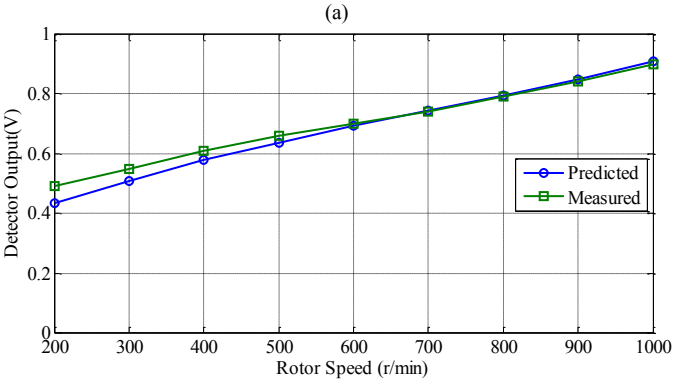

(b)

Fig. 19: Comparison of measured and predicted detector output at i_q =6A, with varying speeds at (a) 2 turn fault and (b) 20 turn fault

Fig. 19 (a) shows the comparison of predicted and actual detector output for 2 turn fault. Fig. 19 (b) shows the comparison of predicted and actual detector output for 20 turn fault. It is to be noted that the high frequency admittance was measured using LCR meter with a very low current excitation (20mA). As load current changes it is expected that the inductance of the machine will change due to saturation which will affect the PWM ripple currents. Further, there is also a 4% variation of individual phase impedances at 10 kHz as measured using the impedance analyzer. Another effect that can cause difference is the contactor impedance used to create the turn fault. However, as previously pointed out the variation are to be expected and can be cancelled out as explained in the next section.

VII. Fault Detection

In order to detect turn fault, it is required that the variation of PWM ripple current under healthy operation with varying speed and loading be accounted and removed. This is particularly true in the case of faults with low number of short-circuited turns, where the increase in the PWM ripple current due to the fault is low. By way of example, the variation of measured phase-4 detector output (phase with turn fault) with speed and current under healthy and 2-turn fault operation is shown in Fig. 20(a). It can be observed that at higher speed (>600 r/min) there exists a clear difference between the healthy and fault operation in the detector output, however at lower speeds there exists some overlap between the healthy and fault cases. As the speed and load are varied the overall inverter command voltage increases and this causes an increase in the PWM ripple current, which makes fault detection using a simple threshold comparison difficult.

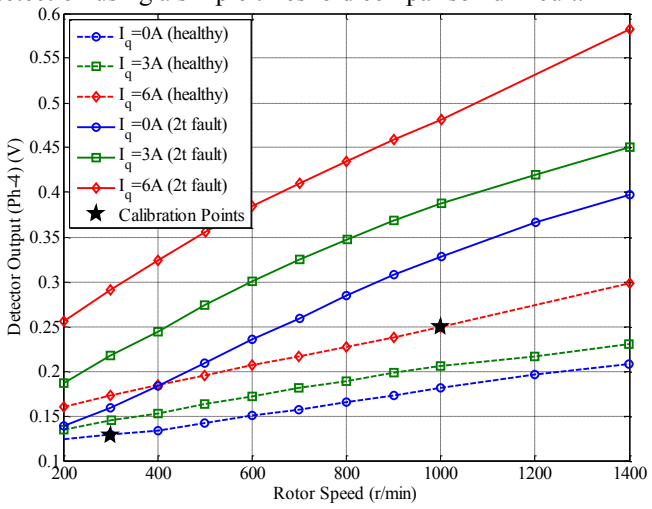

(a)

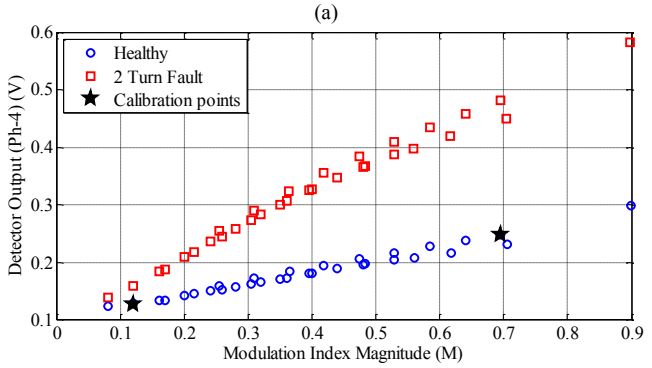

(b)

Fig. 20: Variation of measured detector output (ph-4) with load current (0%, 50%, 100%) and speed plotted with respect to (a) speed, (b) modulation index. Dashed curves refer to healthy operation and solid lines refer to 2-turn fault condition. Stared points are the selected test points for detector calibration.

Harmonic current under healthy condition is a function of the modulation index magnitude as given by (13)-(14) irrespective of the current (i_d or i_q) or speed. In order to eliminate the ripple current contribution due to healthy operation of the machine, a simple algorithm based on linear curve fit is proposed. It can be observed from Fig. 20(b) that the detector output varies almost linearly with the fundamental

modulation index. Detector data from 2 test points corresponding to two different modulation indexes at two different speeds (300 and 1000 r/min) and current loading (0A and 6A) under healthy operation as shown in Fig. 20 are extracted and a linear fit is performed using (15).

$$\text{detector}_h = a_4 M + b_4 \tag{15}$$

Where, M is defined by (16) and V_{d1} and V_{q1} are the controller fundamental frequency dq command voltages.

$$M = \frac{\sqrt{{V_{d1}}^2 + {V_{q1}}^2}}{V_{dc}/2} \tag{16}$$

The 2 fitted parameters are a_4 = 0.208V and b_4 = 0.103V. Using the obtained parameters, calibrated detector output for phase-4 is generated by using (17).

$$\text{calibrated detector} = \text{detector} - \text{detector}_h \tag{17}$$

The output of the calibrated detector is shown in Fig. 21 for the same current and speed variation under healthy and 2-turn fault. It can be observed that the variation of the detector under healthy operation due to load and speed has been effectively cancelled. Slight error does exists however, as can be observed in the healthy case with i_q=0, 3A at higher speed due to use of the simple calibration technique. More advanced calibration algorithms using neural networks or lookup tables can also be used, which can result in improved sensitivity and robustness of the detection.

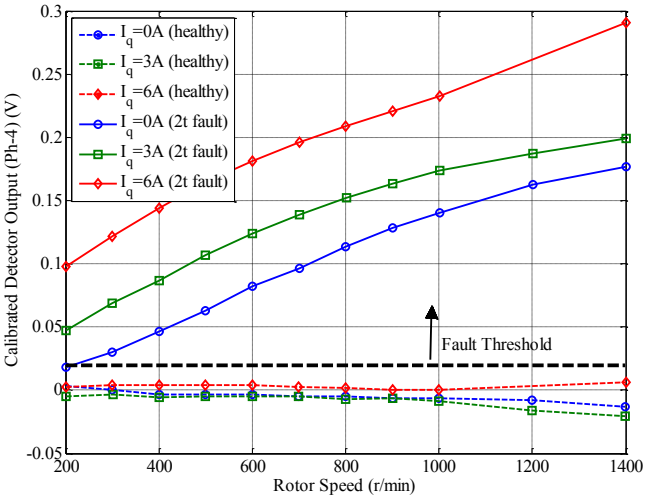

Fig. 21: Variation of calibrated detector output (ph-4) at various loading (0%,50%,100%) with varying speed. Dashed curves refer to healthy motor operation and solid lines refer to 2-turn fault condition.

Under ideal conditions, one set of the fitted parameters can be used to calibrate all the phases. However, due to differences in individual detector channels and machine asymmetry, the proposed calibration procedure is performed for the other phases as well, resulting in a total of 10 constants required to perform calibration for all phases. It is to be noted that only 2 operating point data are needed to completely determine all the 10 constants.

Using a threshold value of 0.02, the calibrated detector output can be employed to classify healthy or faulted operation as shown in Fig. 21. A higher value of detector threshold will be more robust to detector noise at the expense of low sensitivity at lower speed and fault currents.

Fig. 22 shows the calibrated detector output of all the phases for 2 turn fault for i_q=0A which is the worst case scenario for fault detection due to the low fault signature. It can be observed in Fig. 22 that by quantifying the maximum of the detector outputs of all the phases, the faulted phase (ph-4) can be readily identified. Similar results are obtained for other current loading but not included due to the space limit.

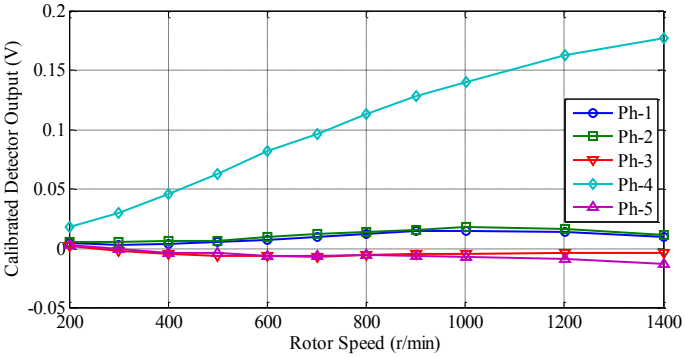

Fig. 22: Variation of all calibrated detector outputs at i_q=0A with varying speed under 2 turn fault. Ph-4 is the faulted phase.

VIII. Conclusion

A new technique to detect turn fault using PWM ripple currents has been described in the paper. A machine model based on measured high frequency winding parameters to capture the high frequency behavior of the winding has been developed. Based on the analytical simulations, a detector circuit to extract the PWM ripple current has been designed. Experiments confirm that PWM ripple based method can be used to successfully detect turn faults in the machine. A simple and effective software calibration technique has been proposed to cancel the ripple current expected under healthy operation to obtain a calibrated detector output. Application of simple fault threshold on the calibrated detector has been shown to be sufficient to determine fault. By quantifying the maximum of the detector outputs of all the phases, the faulted phase can be identified.

PWM current ripple based fault detection can be easily incorporated into drives as an add-on card and connected to controller using analog input channels. Since most of the high frequency signal processing is done on the card, a low frequency sampling of the detector output by the controller is sufficient. Test show that the detection can be performed at low speeds and low currents which are of advantage compared to fundamental component based methods which have difficulty due to low signal to noise ratio.

References

[1] Z. Q. Zhu and D. Howe, "Electrical Machines and Drives for Electric, Hybrid, and Fuel Cell Vehicles," *Proc. IEEE*, vol. 95, no. 4, pp. 746 – 765, Apr. 2007.

[2] K. T. Chau, C. C. Chan, and C. Liu, "Overview of Permanent-Magnet Brushless Drives for Electric and Hybrid Electric Vehicles," *IEEE Trans. Ind. Electron.*, vol. 55, no. 6, pp. 2246–2257, Jun. 2008.

[3] T. G. Habetler and Y. Lee, "Current-based condition monitoring and fault tolerant operation for electric machines in automotive applications," in *International Conference on Electrical Machines and Systems, 2007. ICEMS*, 2007, pp. 2011 –2016.

[4] "OnStar Vehicle Diagnostics." [Online]. Available: https://www.onstar.com/web/portal/systemdetails?g=1#engine. [Accessed: 19-Nov-2014].

[5] "Improved Motors for Utility Applications, Volume 1: Industry Assessment Study: Update and Analysis," EPRI, Technical Report EL-4286-V1, Oct. 1982.

[6] "Report of Large Motor Reliability Survey of Industrial and Commercial Installations, Part I," *IEEE Trans. Ind. Appl.*, vol. IA-21, no. 4, pp. 853–864, 1985.

[7] "Report of Large Motor Reliability Survey of Industrial and Commercial Installations, Part II," *IEEE Trans. Ind. Appl.*, vol. IA-21, no. 4, pp. 865–872, 1985.

[8] O. V. Thorsen and M. Dalva, "A survey of faults on induction motors in offshore oil industry, petrochemical industry, gas terminals, and oil refineries," *IEEE Trans. Ind. Appl.*, vol. 31, no. 5, pp. 1186–1196, 1995.

[9] A. H. Bonnett and C. Yung, "Increased Efficiency Versus Increased Reliability," *IEEE Ind. Appl. Mag.*, vol. 14, no. 1, pp. 29–36, 2008.

[10] Z. Sun, J. Wang, D. Howe, and G. Jewell, "Analytical Prediction of the Short-Circuit Current in Fault-Tolerant Permanent-Magnet Machines," *IEEE Trans. Ind. Electron.*, vol. 55, no. 12, pp. 4210 – 4217, Dec. 2008.

[11] A. H. Bonnett and G. C. Soukup, "Cause and analysis of stator and rotor failures in three-phase squirrel-cage induction motors," *IEEE Trans. Ind. Appl.*, vol. 28, no. 4, pp. 921–937, 1992.

[12] Y.-S. Lee, K.-T. Kim, and J. Hur, "Finite-Element Analysis of the Demagnetization of IPM-Type BLDC Motor With Stator Turn Fault," *IEEE Trans. Magn.*, vol. 50, no. 2, pp. 889–892, Feb. 2014.

[13] A. Gandhi, T. Corrigan, and L. Parsa, "Recent Advances in Modeling and Online Detection of Stator Interturn Faults in Electrical Motors," *IEEE Trans. Ind. Electron.*, vol. 58, no. 5, pp. 1564–1575, 2011.

[14] M. Riera-Guasp, J. A. Antonino-Daviu, and G.-A. Capolino, "Advances in Electrical Machine, Power Electronic, and Drive Condition Monitoring and Fault Detection: State of the Art," *IEEE Trans. Ind. Electron.*, vol. 62, no. 3, pp. 1746–1759, Mar. 2015.

[15] Y. Lee and T. G. Habetler, "An On-Line Stator Turn Fault Detection Method for Interior PM Synchronous Motor Drives," presented at the APEC 2007 - Twenty Second Annual IEEE Applied Power Electronics Conference, 2007, pp. 825–831.

[16] C. Bianchini, E. Fornasiero, T. N. Matzen, N. Bianchi, and A. Bellini, "Fault detection of a five-phase Permanent-Magnet machine," in *34th Annual Conference of IEEE Industrial Electronics, 2008. IECON 2008*, 2008, pp. 1200–1205.

[17] J. Quiroga, L. Liu, and D. A. Cartes, "Fuzzy logic based fault detection of PMSM stator winding short under load fluctuation using negative sequence analysis," in *American Control Conference, 2008*, 2008, pp. 4262 –4267.

[18] I. Jeong, B. J. Hyon, and K. Nam, "Dynamic Modeling and Control for SPMSMs With Internal Turn Short Fault," *IEEE Trans. Power Electron.*, vol. 28, no. 7, pp. 3495–3508, 2013.

[19] T. Boileau, N. Leboeuf, B. Nahid-Mobarakeh, and F. Meibody-Tabar, "Synchronous Demodulation of Control Voltages for Stator Interturn Fault Detection in PMSM," *IEEE Trans. Power Electron.*, vol. 28, no. 12, pp. 5647–5654, Dec. 2013.

[20] F. Immovilli, C. Bianchini, E. Lorenzani, A. Bellini, and E. Fornasiero, "Evaluation of Combined Reference Frame Transformation for Interturn Fault Detection in Permanent-Magnet Multiphase Machines," *IEEE Trans. Ind. Electron.*, vol. 62, no. 3, pp. 1912–1920, Mar. 2015.

[21] N. Leboeuf, T. Boileau, B. Nahid-Mobarakeh, N. Takorabet, F. Meibody-Tabar, and G. Clerc, "Effects of Imperfect Manufacturing Process on Electromagnetic Performance and Online Interturn Fault Detection in PMSMs," *IEEE Trans. Ind. Electron.*, vol. 62, no. 6, pp. 3388–3398, Jun. 2015.

[22] F. Briz, M. W. Degner, A. Zamarron, and J. M. Guerrero, "Online stator winding fault diagnosis in inverter-fed AC machines using high-frequency signal injection," *IEEE Trans. Ind. Appl.*, vol. 39, no. 4, pp. 1109–1117, 2003.

[23] F. Briz, M. W. Degner, P. Garcia, and A. B. Diez, "High-Frequency Carrier-Signal Voltage Selection for Stator Winding Fault Diagnosis in Inverter-Fed AC Machines," *IEEE Trans. Ind. Electron.*, vol. 55, no. 12, pp. 4181–4190, 2008.

[24] J. Arellano-Padilla, M. Sumner, and C. Gerada, "Winding condition monitoring schemefor a permanent magnet machine using high-frequency injection," *IET Electr. Power Appl.*, vol. 5, no. 1, pp. 89–99, 2011.

[25] B.-M. Ebrahimi and J. Faiz, "Feature Extraction for Short-Circuit Fault Detection in Permanent-Magnet Synchronous Motors Using Stator-Current Monitoring," *IEEE Trans. Power Electron.*, vol. 25, no. 10, pp. 2673–2682, 2010.

[26] J. A. Rosero, L. Romeral, J. A. Ortega, and E. Rosero, "Short-Circuit Detection by Means of Empirical Mode Decomposition and Wigner-Ville Distribution for PMSM Running Under Dynamic Condition," *IEEE Trans. Ind. Electron.*, vol. 56, no. 11, pp. 4534–4547, Nov. 2009.

[27] J. Park and J. Hur, "Detection of Inter-Turn and Dynamic Eccentricity Faults using Stator Current Frequency Pattern in IPM-type BLDC Motors," *IEEE Trans. Ind. Electron.*, vol. PP, no. 99, pp. 1–1, 2015.

[28] S. Kim, J.-I. Ha, and S.-K. Sul, "PWM Switching Frequency Signal Injection Sensorless Method in IPMSM," *IEEE Trans. Ind. Appl.*, vol. 48, no. 5, pp. 1576–1587, Sep. 2012.

[29] A. A. Khan and O. Mohammed, "Neural network based modeling of audible noise for high frequency injection based position estimation for PM synchronous motors at low and zero speed," in *IEEE Electric Ship Technologies Symposium, 2009. ESTS 2009*, 2009, pp. 119–122.

[30] B. Sen and J. Wang, "Stator inter-turn fault detection in SPM machines using PWM ripple current measurement," in *7th IET International Conference on Power Electronics, Machines and Drives (PEMD 2014)*, 2014, pp. 1–6.

[31] D. G. Holmes and T. A. Lipo, *Pulse Width Modulation for Power Converters: Principles and Practice*. Wiley-IEEE Press, 2003.

[32] L. Parsa and H. A. Toliyat, "Five-Phase Permanent-Magnet Motor Drives," *IEEE Trans. Ind. Appl.*, vol. 41, no. 1, pp. 30–37, Jan. 2005.

[33] "LTC1968 - Precision Wide Bandwidth, RMS-to-DC Converter - Linear Technology." [Online]. Available: http://www.linear.com/product/LTC1968. [Accessed: 09-Jan-2014].

Bhaskar Sen (S'11) received the B.E. degree from Delhi College of Engineering, Delhi, India in 2003 and the M.Tech. degree from Indian Institute of Technology, Kanpur, India in 2006. From 2006 to 2011, he was with GE Global Research, Bangalore, India. Since 2011 he has been working towards the Ph.D. degree in the University of Sheffield, UK. His current research interests include electrical machine fault modelling, machine fault detection and fault tolerant drives.

Jiabin Wang (SM'03) received the B.Eng. and M.Eng. degrees from Jiangsu University of Science and Technology, Zhengjiang, China, in 1982 and 1986, respectively, and the Ph.D. degree from the University of East London, London, U.K., in 1996, all in electrical and electronic engineering.

Currently, he is a Professor in Electrical Engineering at the University of Sheffield, Sheffield, U.K. From 1986 to 1991, he was with the Department of Electrical Engineering at Jiangsu University of Science and Technology, where he was appointed a Lecturer in 1987 and an Associated Professor in 1990. He was a Postdoctoral Research Associate at the University of Sheffield, Sheffield, U.K., from 1996 to 1997, and a Senior Lecturer at the University of East London from 1998 to 2001. His research interests range from motion control and electromechanical energy conversion devices to electric drives for applications in automotive, renewable energy, household appliances and aerospace sectors.

Dr. Wang is a fellow of the Institute of Engineering and Technology, UK.